

High-Temperature Oxidation Behavior of Wrought and Additive Manufactured Ni-based Alloys in Direct-Fired Supercritical CO₂ Power Cycle Environments

Casey S. Carney
NETL Support Contractor
National Energy Technology Laboratory
Albany, OR

Richard P. Oleksak
Research Materials Scientist
National Energy Technology Laboratory
Albany, OR

Nicholas Lamprinakos
Graduate Student
Carnegie Mellon University,
Department of Materials Science and
Engineering
Pittsburgh, PA

Anthony D. Rollett
Professor
Carnegie Mellon University,
Department of Materials Science and
Engineering
Pittsburgh, PA

Ömer N. Doğan
Materials Research Engineer
National Energy Technology Laboratory
Albany, OR

ABSTRACT

Materials selection is a key concern for corrosion resistance in elevated temperature and pressure direct-fired supercritical CO₂ (sCO₂) power cycles. Herein, the wrought product form of alloy H282, as well as several additional nickel-based commercial alloys (230, 263, 617, 625, 740H), were exposed to direct-fired supercritical CO₂ conditions (95CO₂ – 4H₂O – 1O₂) at 750 °C and 20 MPa for over 2,000 h. Additionally, additive manufactured (AM) 282 produced by laser powder bed fusion (LPBF) were also included in the exposures. This paper focuses primarily on the differences observed in the degradation behavior of the wrought and additively manufactured materials. AM samples in the as-printed state were found to form less protective oxide scales resulting in higher oxidation rates compared to wrought samples. However, applying a 600 grit surface finish to the AM samples modified the oxidation behavior to closely resemble that of the wrought material. The AM samples formed Mo-rich carbides in the alloy beneath the oxide following sCO₂ exposure, implying potentially higher levels of carbon uptake relative to the wrought material. Conversely, the AM samples seemed to be less affected by water-assisted oxide volatilization compared to the wrought material. The results are discussed in terms of the potential compatibility issues that may arise when using Ni-based alloys in the hot portions of direct-fired sCO₂ power cycles, particularly in the case of thin-walled components.

INTRODUCTION

Supercritical CO₂ (sCO₂) cycles offer the potential for high efficiency power generation. The materials selected for equipment construction for these power cycles is critical, as they need to survive the harsh conditions of high temperatures, high pressures, and corrosive environments. Ni-based superalloys have been shown to be good material candidates [1]. Direct-fired sCO₂ power cycles differ from a pure (indirect) CO₂ power cycle as the working fluid contains some of the products from oxy-fuel combustion, namely water and oxygen. While the presence of low levels of water and oxygen within a pure CO₂ combustion environment has been shown to have minimal effect on material oxidation at ambient pressures [2-5], there is limited data on high-pressure oxidation with these impurities. What little data does exist suggests increased corrosion effects at elevated pressures [6-10]. Additionally, chromia scale volatilization during direct-fired sCO₂ exposure has also been observed [11]. Further investigation into the oxidation of Ni-based superalloys within direct-fired supercritical CO₂ environments is necessary for a thorough evaluation of the applicability of these materials.

Additive manufacturing (AM) by laser powder bed fusion (LPBF) are production methods with high reproducibility and dimensional accuracy and are an area of current interest [12-19]. Designs for sCO₂ power systems will require construction of compact components with narrow fluid flow paths, thus AM production methods could be useful for these designs [20-22]. However, possible effects of the AM process on environmental performance of candidate materials for sCO₂ power system is largely unknown.

EXPERIMENTAL

Additively manufactured H282 test coupons were produced from H282 powder using various laser powder bed fusion process parameter sets. Three varieties of AM test coupons were produced with different laser velocities and power: S1 (959 mm/s – 250 W), S2 (1,366 mm/s – 350 W), and S3 (1,772 mm/s – 370 W). All three AM varieties had densities >99.9%. Test coupons were printed with dimensions of 15 mm x 10 mm x 1.2 mm, with a 4 mm diameter hole in the top for sample suspension within the autoclave. After printing, all samples underwent a three-step heat treatment under argon: (1) 1,250 °C for 2 h (solution annealing), (2) 899 °C for 4 h (aging), and (3) 788 °C for 8 h (aging). Samples were exposed to supercritical conditions in this “As Printed” (AP) state and after a “Surface Finishing” (SF) step using 600 grit SiC paper. Experimental test coupons were also machined and from commercially available wrought Ni-based alloys (230, 263, 282, 617, 625, 740H) and similarly surface finished using 600 grit SiC paper. The compositions of the alloys utilized in this study are listed in Table 1.

Alloy	Ni	Cr	Fe	Co	Mo	W	Al	Si	Ti	Mn	Nb	C (ppm)
230	60.4	21.3	0.4	0.3	1.2	14.8	0.4	0.45	0.01	0.4	0.04	903
263	51.1	19.9	0.01	20	5.6	-	0.4	0.28	2.1	0.5	0.1	560
282	58.4	19.2	0.1	10.2	8.4	-	1.3	0.04	2.1	0.1	0.02	600
617	55.1	21.8	0.4	11.4	9.6	-	1	0.02	0.5	0.04	0.03	843
625	61	21.4	4.4	0.1	8.4	-	0.2	0.35	0.3	0.1	3.3	181
740H	50.6	24.5	-	20.1	0.3	-	1.2	0.12	1.4	0.2	1.5	238

Table 1. Compositions of the tested Ni-based superalloys.

These coupons were exposed to direct-fired supercritical conditions of $95\text{CO}_2 - 4\text{H}_2\text{O} - 1\text{O}_2$ (by mole) at $750\text{ }^\circ\text{C}$ and 200 bar in a vertical autoclave (H230) (Marks Brothers) with three zone heat control (Thermcraft). A vertical Inconel 718 sample tree hanging downward into the autoclave was used to suspend the coupons within the autoclave, with hooks extending horizontally, as shown in Figure 1. Four baffles were affixed above the sample tree for hot zone heat insulation. The autoclave diameter was 5.7 cm with a depth of 38.7 cm below the lowest baffle. A liquid phase dual head pump (Supercritical Flow Technologies SFT-10) was used to pressurize and flow CO_2 (high purity 99.999%) at a rate of 2.0 mL/min (liquid volume), yielding a flow velocity of about 0.8 cm/min. The mixed fluid flow was injected through the sample rack near the bottom of the autoclave, then flowed vertically upwards through the hot zone. The autoclave was heated under a static argon atmosphere to $750\text{ }^\circ\text{C}$, and then CO_2 was pumped into the system at a rate of 6.0 mL/min; as the pressure approached 200 bar, the flow rate was reduced to 2.0 mL/min. System pressure was controlled with an adjustable back-pressure regulator and regularly cycled around 200 ± 5 bar. Once the autoclave conditions stabilized at $750\text{ }^\circ\text{C}/200$ bar, water and oxygen were fed at pressure to the system. Reverse osmosis deionized water was injected with a single head liquid pump (Teledyne SSI Lab Alliance Series II) at a rate of 0.037 mL/min. A pneumatic booster pump (Haskel AG-75) was used to feed a 20% O_2/Ar mixture at a rate of 0.111 mL/min. Test coupons were exposed in batch times of 300–500 h and were weighed with a Mettler analytical balance pre-exposure and after each individual exposure test. Samples were removed for microscopy at 1,500 h, but mass tracking exposure tests were further carried out until at least 1,900 h.

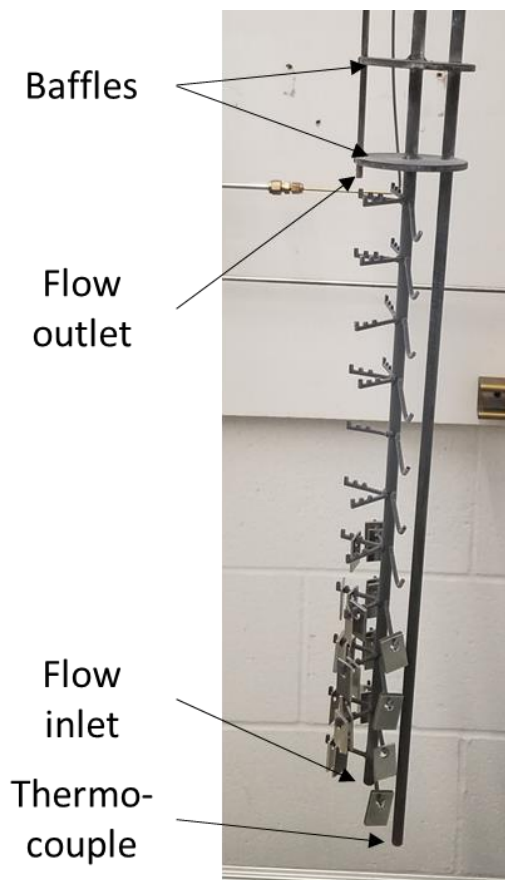


Figure 1. Sample tree for suspending samples within the supercritical autoclave.

The test coupons were also exposed at ambient pressure to a flowing direct-fired environment ($95\text{CO}_2 - 4\text{H}_2\text{O} - 1\text{O}_2$) at $750\text{ }^\circ\text{C}$ in a horizontal tubular reactor heated by a Thermcraft three-zone control box furnace. Reverse osmosis deionized water was fed to the tube with a syringe pump. The combined fluid flow rate was 263 sccm (0.32 kg/h), yielding a 25 cm/min gas velocity inside the tube and a test volume change every 12 s. The coupons were suspended from a horizontal sample rack (Figure 2). Oxygen levels were monitored with a Materials Technology International Corporation Trace Oxygen Analyzer (model W1000-LD).

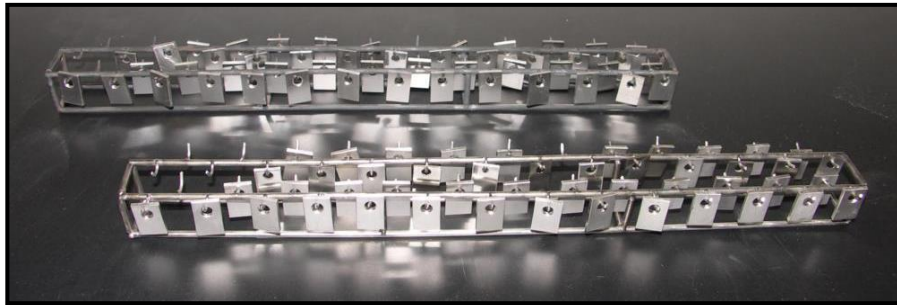


Figure 2. Horizontal rack for suspending samples within a horizontal tube furnace for the ambient pressure exposures.

Micrographs of all coupons were generated with an FEI Inspect F50 SEM. The coupons were copper coated prior to sectioning and mounting for cross-sectional imaging. This process provided verification that no part of the oxide layer was lost during the sample preparation process while copper was still visible in the cross-section. To assist with carbide identification, samples were etched with Murakami's reagent prior to additional microscopy observations.

RESULTS AND DISCUSSION

The general oxidation behavior of the three types of AM samples exposed to direct-fired sCO_2 are shown in relatively low magnification SEM images in Figure 3. The two samples that were surface finished prior to exposure have a relatively smooth and uniform oxidation layer. The AP

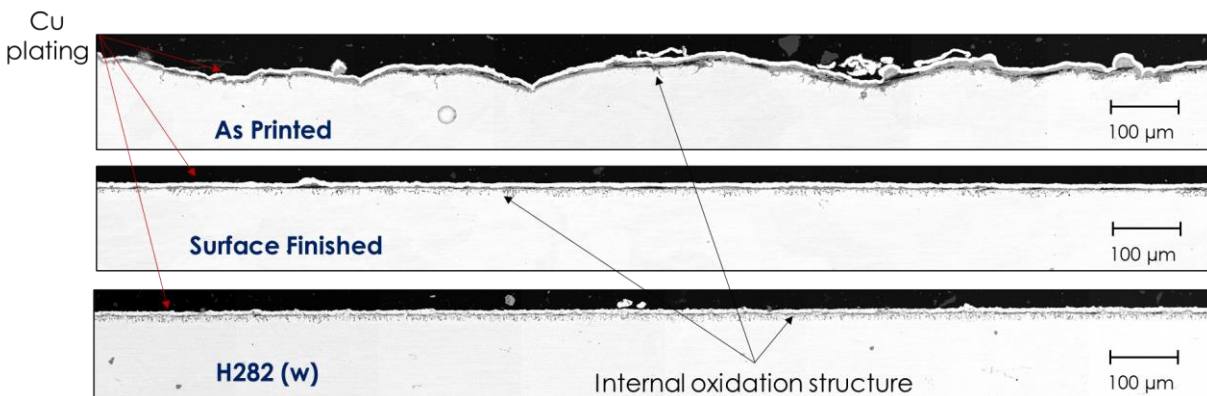


Figure 3. SEM image of bulk oxide behavior of the AM H282 samples compared to wrought H282 exposed to direct-fired sCO_2 at 200 bar.

sample that was not surface finished has a more uneven and variable thickness oxide layer. The AP sample also has a thicker oxide layer than the two other samples (that were both surface finished) and has a less fully developed internal oxidation structure. Both samples that were surface finished also show much more consistent internal oxidation regions, both in terms of structure and depth. There was little observable difference between the SF and the wrought H282 sample.

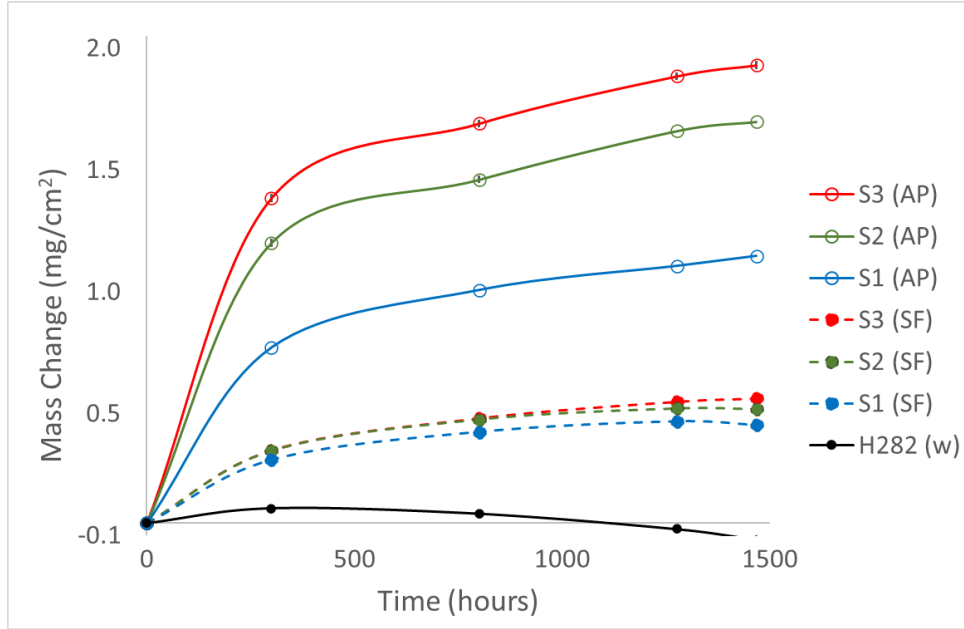
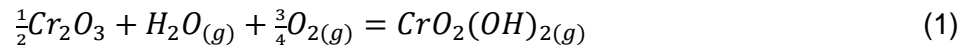


Figure 4. Mass changes for AM and wrought H282 in direct-fired sCO₂ at 200 bar.

The mass change results for AM samples are presented in Figure 4. The surface finishing step had a definite effect on oxidation, as mass gains were greatly reduced for these samples. Overall mass gain varied directly with the AM production laser scan speed, although this behavior was more prevalent for the AP samples. Interestingly, mass gains were lowest for the wrought H282 samples, eventually resulting in negative mass gains at longer exposure times. This behavior is likely not the result of oxide spallation, but rather water vapor assisted chromia volatilization, as described previously [11]. At elevated pressures in the presence of moisture, the water can volatilize oxidized chromia scale into the fluid [23, 24] flow stream.



In this manner, even though oxidation did occur, simple mass measurements cannot fully account for the oxidation process.

For a diffusion-controlled surface reaction, such as oxidation of metal surfaces, the reaction progress can be described by parabolic kinetics:

$$k_p = \frac{\Delta m^2}{2t} \quad (2)$$

where k_p is the parabolic rate constant ($g^2 cm^{-4} s^{-1}$), Δm is the mass change ($g cm^{-2}$), and t is time (s). Equation 1 can be rewritten in a linear plottable form as:

$$\Delta m = \sqrt{2k_p t} \quad (3)$$

where a plot of Δm vs. the square root of time will be linear if parabolic kinetics are valid. The parabolic rate constant k_p can then be computed from the slope of that plot. Figure 5 shows this analysis for the AP and SF samples. For these AM samples, parabolic kinetics were obeyed after an initial induction period of 300 h. For a given AM sample preparation method (AP vs. SF) there were differing overall mass gains for each of the three laser speed production methods. However, the parabolic rate constant k_p was the same for each, suggesting only a difference in the extent of the initial transient oxidation step. Once the passivating oxide layer was developed for each sample, continued oxidation rates were the same for a given sample preparation method. The $\log k_p$ for the SF samples was -13.9 ± 0.1 , while the $\log k_p$ for the AP samples was -13.1 ± 0.2 . As such, continued oxidation rates were slower after the surface finishing step was applied to the samples (a more negative $\log k_p$ value is representative of a slower reaction).

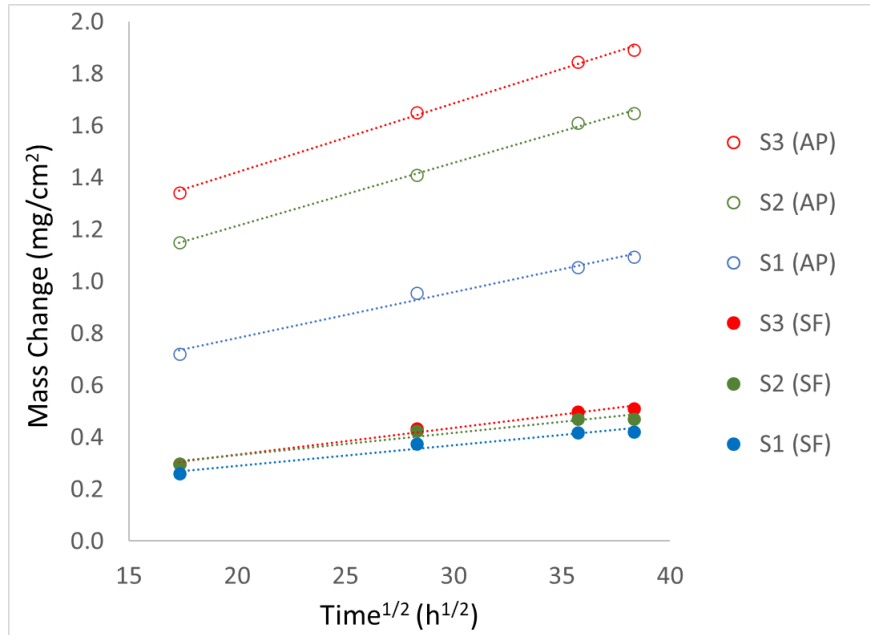


Figure 5. Parabolic kinetic verification plots for AM and wrought H282 in direct-fired $s\text{CO}_2$.

Cross-sectional micrographs of AM samples are presented in Figure 6. There are significant differences between the “As Printed” and “Surface Finished” samples. The SF samples have much thinner and homogeneous oxide layers, which agrees with the mass change results. Internal oxidation structures are deeper and more consistent for the SF samples. In addition to simply smoothing the surface of samples, the surface finishing process introduces residual stresses (dislocations) into the near surface of the alloy, which can act as fast diffusion paths for Cr and promote early development of a passivating chromia layer [25]. Conversely, the AP samples, which lack these high dislocation densities near the surface of the sample, struggle to establish a chromia layer. In addition, the increased surface roughness of the AP samples may also play a role in inhibiting formation of the chromia layer. The result is AP samples that exhibit an irregular duplex oxide scale compared to SF samples.

One notable observation in the micrographs of AM samples is the presence of subsurface white particles/precipitates beneath the oxide layer that extend about 20–30 μm into the alloy. Their close proximity to the alloy surface suggests they are associated with the exposure and not

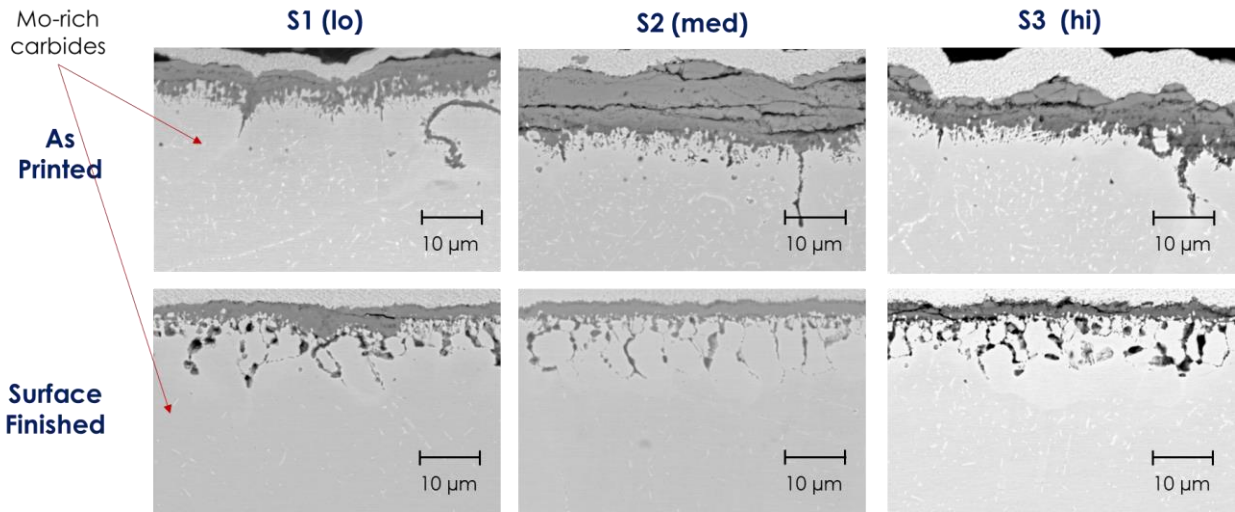


Figure 6. SEM micrographs of the AM H282 coupons exposed to direct-fired sCO₂ at 200 bar.

simply a consequence of thermal aging of the alloy. These structures appear to be more prevalent within the AP samples, but they are also found within the SF samples. Figure 7 shows the energy dispersive X-ray spectroscopy (EDS) maps for the AP samples and the SF samples, respectively. The AP samples reveal a duplex oxide scale, with an outer layer rich in Ni, Co, and Fe and an inner Cr-rich layer. Conversely, the SF oxide scale is much thinner and contains only a single, Cr-rich oxide layer. These images align with the mass change results and further indicate that while the SF samples were able to quickly form a protective chromia layer, the AP samples were not, resulting in the duplex oxide scale. The EDS maps more clearly indicate the presence of the sub-surface particulates, and reveal that they are enriched in Mo.

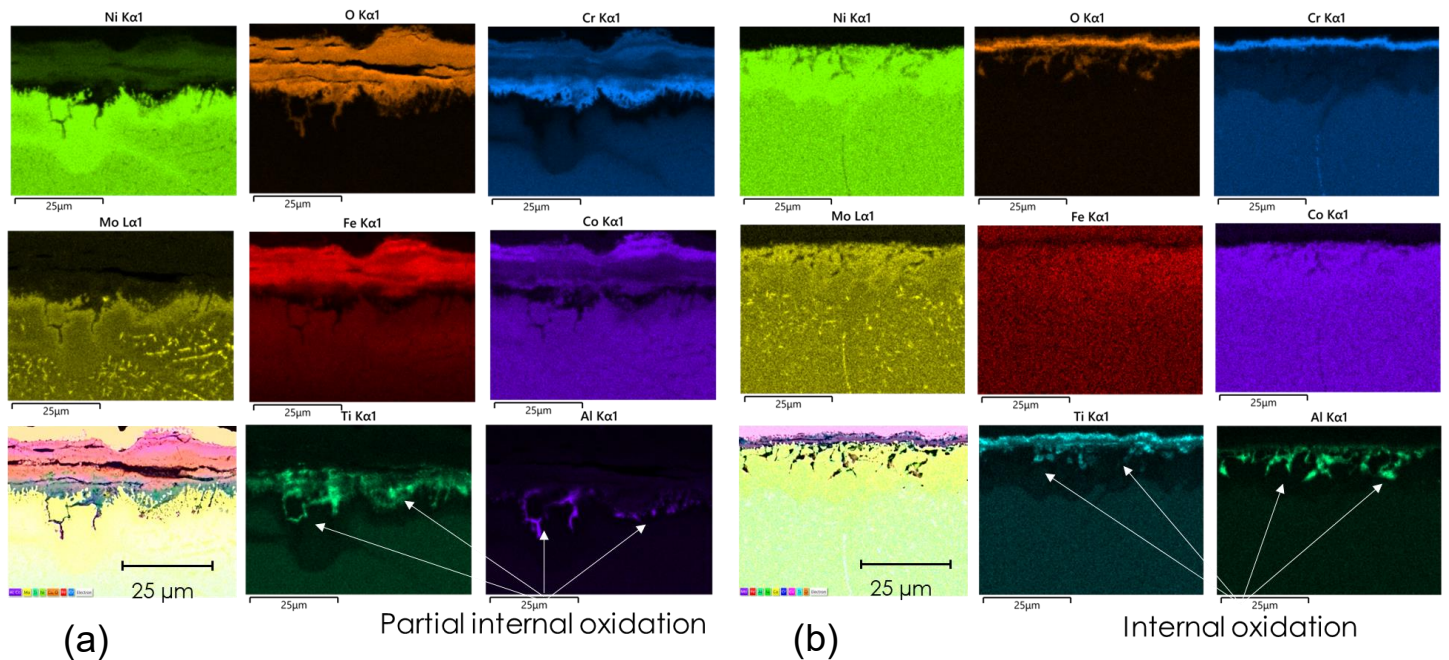


Figure 7. Elemental mapping of an AM AP test coupon (a) and AM SF test coupon (b) exposed to direct-fired sCO₂ at 200 bar.

These Mo-rich structures were suspected to be Mo-rich carbides produced from carbon uptake (carburization) from the CO₂ environment during the direct-fired exposure. To assess for this possibility, the samples were chemically etched to reveal metal carbides in the alloy. Figure 8 shows the etched backscatter SEM images of both the AP and SF AM test coupons. Here the carbides are clearly denoted as dark particles in the subsurface of the alloy. As before, qualitatively carbide concentration appears to be higher for the AP samples, but they are also still clearly present in the SF samples.

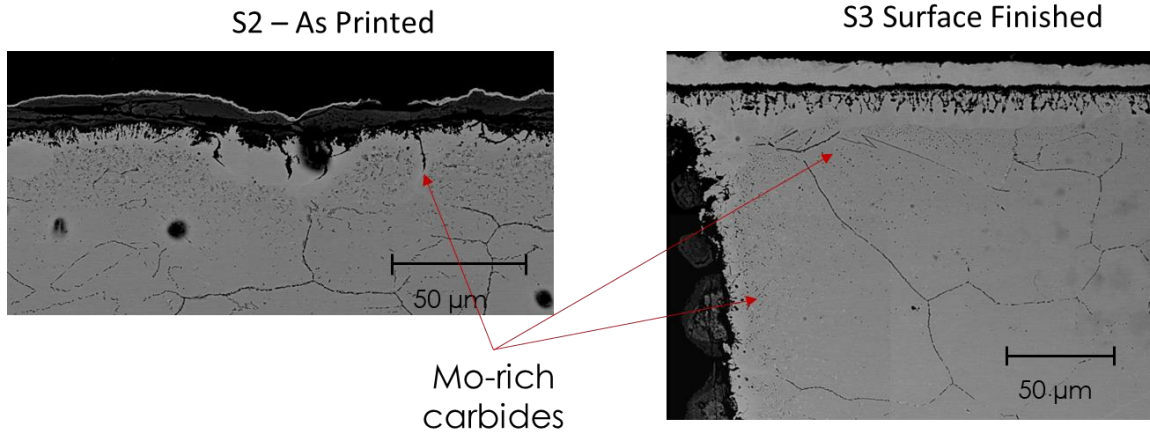


Figure 8. Etched SEM images of AM samples exposed to direct-fired sCO₂ at 200 bar.

The AM samples were also compared to wrought H282. Figure 9 compares etched SEM micrographs between AM SF and wrought H282. The oxide layers and internal oxidation structures are similar between the two, with the wrought H282 having a slightly thinner oxide layer. This is likely due to increased chromia scale volatilization in wrought H282, as described above with the mass change results. However, there is no evidence of the Mo-rich carbides within the wrought H282 samples in the SEM micrographs or EDS maps (Figure 10). The etched SEM micrographs (Figure 9) do show small amounts of possible carbides in the wrought H282, but in much lower concentrations than found in the AM SF sample. While further confirmation is required, the absence of any corresponding Mo enrichment in the EDS maps suggests the carbides in wrought H282 may instead be Cr-rich carbides. Such carbides have been observed previous in wrought Ni-based alloys after long-term exposure to high temperature CO₂ environments [26]. The relatively larger amount of carbides in the AM sample compared to the

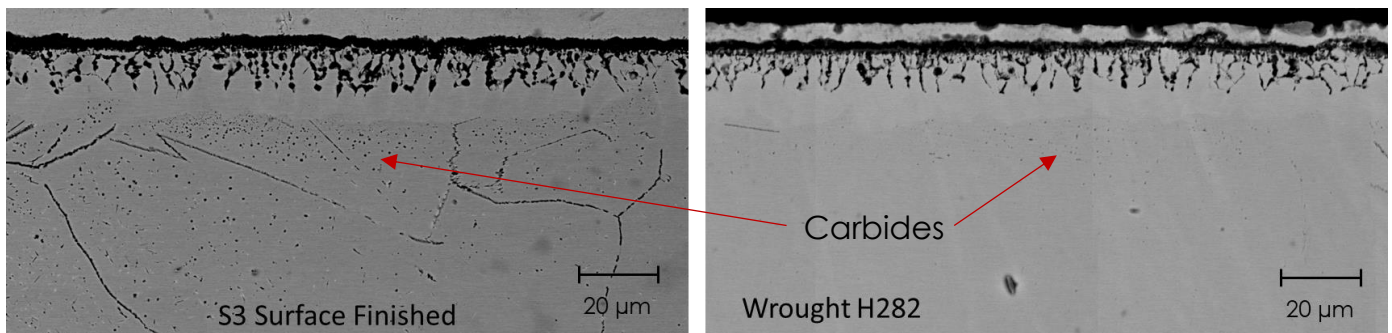


Figure 9. Etched SEM images of AM compared to wrought H282 exposed to direct-fired sCO₂ at 200 bar

wrought sample suggests potentially a larger degree of carbon uptake (carburization) for the AM samples. This may become an important consideration for compact heat exchangers, since thinner metal sections will be more susceptible to carbide precipitation. Depending on the rate of carbon uptake, the extent of carbide precipitation could negatively impact the mechanical properties (e.g., ductility) of the material after prolonged periods.

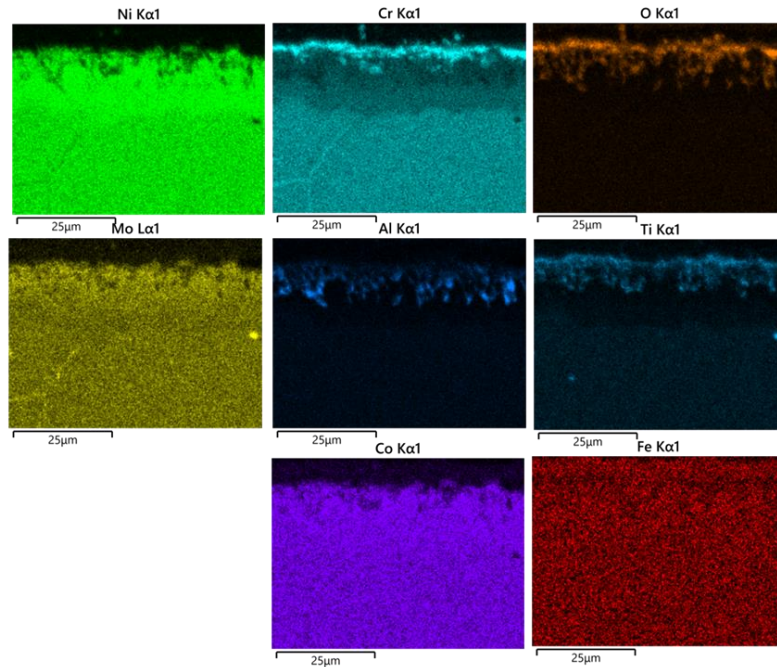


Figure 10. Elemental EDS mapping of wrought H282 exposed to direct-fired sCO₂ at 200 bar.

The oxidation of wrought H282 and other commercial Ni-based alloys under direct-fired conditions at both ambient pressure and supercritical conditions has been discussed in detail by our group previously [11, 27]. As such, the results will only be briefly presented here. Figure 11 shows the mass change comparison between the two pressures. The alloys at ambient pressure all have steady mass gains that follow parabolic kinetic behavior after 500 or 1,000 h. The mass gains for all these alloys are lower at supercritical conditions, and alloys 230 and 625 actually lost mass over the exposure. Even though the mass changes were lower for all exposures at high pressure, cross-sectional micrographs indicated that oxide scales were slightly thicker for the samples exposed at high pressure, and no evidence for oxide spallation was observed [11]. This seemingly incongruous result is again the consequence of the water vapor assisted chromia scale volatilization that occurs at high pressure, but not ambient pressure. As described previously [11], such oxide volatilization processes, which occurred at very low rates in our slow-flowing autoclave test, could proceed at potentially much higher rates in real sCO₂ systems, which operate at significantly higher fluid velocities. This could be especially problematic for compact (e.g., printed circuit) heat exchangers for two reasons. First, chromia volatilization accelerates the rate of Cr depletion in the alloy, meaning that thin-walled components with a relatively smaller reservoir of Cr may eventually become susceptible to breakaway oxidation. Second, any volatilized oxide species would likely re-precipitate (deposit) downstream in the cooler portions of the heat exchanger, leading to potential clogging issues for narrow flow channels. Notably, the clear parabolic oxidation behavior observed in Figure 5 suggests that the

AM samples did not experience measurable levels of chromia volatilization (i.e., no obvious loss of mass of the oxide). Hence, the AM samples may be more resistant to chromia volatilization compared to the wrought material.

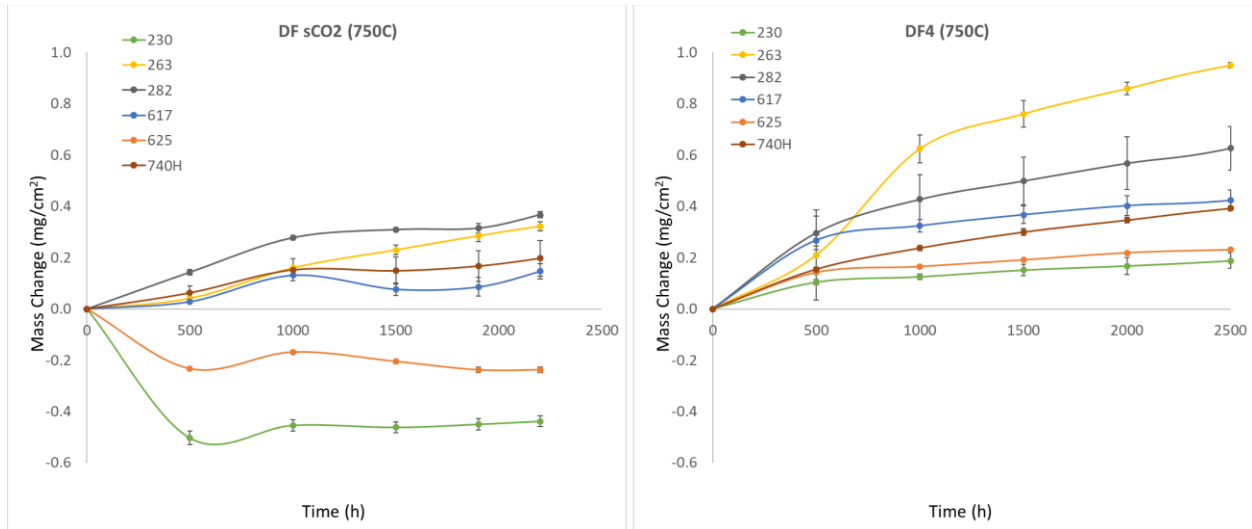


Figure 11. Mass changes for commercial Ni-based alloys in direct-fired sCO₂ at 200 bar (DF sCO₂) compared to ambient pressure direct-fired CO₂ (DF4).

SUMMARY

The oxidation response of additively manufactured (AM) H282 in direct-fired supercritical CO₂ conditions was investigated and compared to the oxidation response of wrought H282. The “As Printed” (AP) samples formed a less protective oxide scale, resulting in higher oxidation rates, relative to the wrought material. A “Surface Finishing” (SF) step was found to have a significant effect on the AM samples, resulting in a more protective oxide scale and lower oxidation rates that were comparable to the wrought material. Notable quantities of Mo-rich carbide particles formed beneath the oxide in the AM samples that were not observed for wrought samples, suggesting that the AM material may be more susceptible to carburization during exposure to direct-fired sCO₂ environments. Conversely, water assisted chromia volatilization observed for wrought H282 (and other wrought Ni-based alloys) was not observed for the AM H282, suggesting the AM materials may be more resistant to this form of degradation. In summary, additive manufacturing and subsequent surface preparation processes can affect the rates of oxidation, carburization, and oxide volatilization of H282, and likely other Ni-based alloys. These factors should be taken into consideration when evaluating materials for direct-fired sCO₂ systems, especially for thin-walled components such as compact heat exchangers.

REFERENCES

1. Oleksak, R.P., Rouillard, F., *Materials performance in CO₂ and supercritical CO₂*, in *Comprehensive Nuclear Materials*, 2nd ed, R.E.S. R.J.M. Konings, Editor. 2020, Elsevier: Oxford. p. 422-451.
2. Huczkowski, P., et al., *Effect of Sulphur on the Oxidation Behaviour of Possible Construction Materials for Heat Exchangers in Oxyfuel Plants in the Temperature Range 550-700 °C*. *Oxidation of Metals*, 2018. **89**(5-6): p. 651-681.
3. Mu, N., et al., *Water Vapor Effects on the Oxidation Behavior of Fe-Cr and Ni-Cr Alloys in Atmospheres Relevant to Oxy-fuel Combustion*. *Oxidation of Metals*, 2012. **78**(3-4): p. 221-237.
4. Oleksak, R.P., et al., *High temperature oxidation of Ni alloys in CO₂ containing impurities*. *Corrosion Science*, 2019. **157**: p. 20-30.
5. Oleksak, R.P., et al., *Temperature-Dependence of Corrosion of Ni-Based Superalloys in Hot CO₂-Rich Gases Containing SO₂ Impurities*. *JOM*, 2020. **72**(5): p. 1822-1829.
6. Lehmusto, J., et al., *The Impact of Impurities on Alloy Behavior in Supercritical CO₂ at 700 °C*. *Oxidation of Metals*, 2020. **94**(1-2): p. 95-111.
7. Li, K.Y., Y.M. Zeng, and J.L. Luo, *Corrosion of SS310 and Alloy 740 in high temperature supercritical CO₂ with impurities H₂O and O₂*. *Corrosion Science*, 2021. **184**.
8. Mahaffey, J., et al., *Corrosion of Alloy Haynes 230 in High Temperature Supercritical Carbon Dioxide with Oxygen Impurity Additions*. *Oxidation of Metals*, 2016. **86**(5-6): p. 567-580.
9. Mahaffey, J., et al., *Effects of CO and O₂ Impurities on Supercritical CO₂ Corrosion of Alloy 625*. *Metallurgical and Materials Transactions A-Physical Metallurgy and Materials Science*, 2018. **49A**(8): p. 3703-3714.
10. Pint, B.A., et al., *Effect of pressure and impurities on oxidation in supercritical CO₂*. *Materials and Corrosion-Werkstoffe Und Korrosion*, 2019. **70**(8): p. 1400-1409.
11. Oleksak, R.P., C.S. Carney, and O.N. Dogan, *Effect of pressure on high-temperature oxidation of Ni alloys in supercritical CO₂ containing impurities*. *Corrosion Science*, 2023. **215**.
12. Blakey-Milner, B., et al., *Metal additive manufacturing in aerospace: A review*. *Materials & Design*, 2021. **209**.
13. Cunningham, R., et al., *Analyzing the effects of powder and post-processing on porosity and properties of electron beam melted Ti-6Al-4V*. *Materials Research Letters*, 2017. **5**(7): p. 516-525.
14. Everton, S.K., et al., *Review of in-situ process monitoring and in-situ metrology for metal additive manufacturing*. *Materials & Design*, 2016. **95**: p. 431-445.
15. Frazier, W.E., *Metal Additive Manufacturing: A Review*. *Journal of Materials Engineering and Performance*, 2014. **23**(6): p. 1917-1928.
16. Gong, G.H., et al., *Research status of laser additive manufacturing for metal: a review*. *Journal of Materials Research and Technology*, 2021. **15**: p. 855-884.
17. Lewandowski, J.J. and M. Seifi, *Metal Additive Manufacturing: A Review of Mechanical Properties*, in *Annual Review of Materials Research*, Vol 46, D.R. Clarke, Editor. 2016. p. 151-186.
18. Seifi, M., et al., *Overview of Materials Qualification Needs for Metal Additive Manufacturing*. *JOM*, 2016. **68**(3): p. 747-764.
19. Slotwinski, J.A., E.J. Garboczi, and K.M. Hebenstreit, *Porosity Measurements and Analysis for Metal Additive Manufacturing Process Control*. *Journal of Research of the National Institute of Standards and Technology*, 2014. **119**: p. 494-528.
20. Kwon, J.S., et al., *Compact heat exchangers for supercritical CO₂ power cycle application*.

- Energy Conversion and Management, 2020. **209**.
21. Magnin, C., et al., *The performance of additively manufactured Haynes 282 in supercritical CO₂*. Materials Science and Engineering A-Structural Materials Properties Microstructure and Processing, 2022. **841**.
 22. Robey, E., et al., *Design optimization of an additively manufactured prototype recuperator for supercritical CO₂ power cycles*. Energy, 2022. **251**.
 23. Opila, E.J., *Volatility of common protective oxides in high-temperature water vapor: Current understanding and unanswered questions*, in *High Temperature Corrosion and Protection of Materials 6, Part 1 and 2, Proceedings*, P. Steinmetz, et al., Editors. 2004. p. 765-773.
 24. Young, D.J. and B.A. Pint, *Chromium volatilization rates from Cr₂O₃ scales into flowing gases containing water vapor*. Oxidation of Metals, 2006. **66**(3-4): p. 137-153.
 25. Oleksak, R.P., Holcomb, G. R., Carney, C. S., Teeter, L., Doğan, Ö. N., *Effect of surface finish on high-temperature oxidation of steels in CO₂, supercritical CO₂, and air*. Oxidation of Metals, 2019. **92**(5-6): p. 525-540.
 26. Oleksak, R.P., Holcomb, G. R., Carney, C. S., & Doğan, Ö. N, *Carburization susceptibility of chromia-forming alloys in high-temperature CO₂*. Corrosion Science, 2022. **206**(110488).
 27. Oleksak, R.P., et al., *High-Temperature Corrosion of Chromia-Forming Ni-Based Alloys in CO₂ Containing Impurities*. High Temperature Corrosion of Materials, 2023.

ACKNOWLEDGEMENTS

This work was performed in support of the U.S. Department of Energy's (DOE) Fossil Energy and Carbon Management's Advanced Energy Materials Program and executed through the National Energy Technology Laboratory (NETL) Research & Innovation Center's Advanced Materials Development Field Work Proposal.

This work was also performed in support of the ARPA-E HITEMMP project titled "High Energy Density Modular Heat Exchangers through Design, Materials Processing, and Manufacturing Innovations."

The authors would like to thank Dennis Burkey for maintenance, assembly, and disassembly of the supercritical autoclave; Matthew Fortner, James Willis, and Dennis Funk for metallography work and SEM sample preparation.

DISCLAIMER

This project was funded by the United States Department of Energy, National Energy Technology Laboratory, in part, through a site support contract. Neither the United States Government nor any agency thereof, nor any of their employees, nor the support contractor, nor any of their employees, makes any warranty, express or implied, or assumes any legal liability or responsibility for the accuracy, completeness, or usefulness of any information, apparatus, product, or process disclosed, or represents that its use would not infringe privately owned rights. Reference herein to any specific commercial product, process, or service by trade name, trademark, manufacturer, or otherwise does not necessarily constitute or imply its endorsement, recommendation, or favoring by the United States Government or any agency thereof. The views and opinions of authors expressed herein do not necessarily state or reflect those of the United States Government or any agency thereof.

